

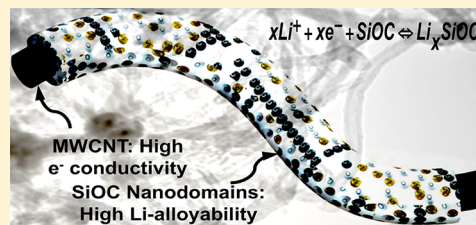
Stable and Efficient Li-Ion Battery Anodes Prepared from Polymer-Derived Silicon Oxycarbide–Carbon Nanotube Shell/Core Composites

R. Bhandavat and G. Singh*

Department of Mechanical and Nuclear Engineering, Kansas State University, Manhattan, Kansas 66506, United States

Supporting Information

ABSTRACT: We demonstrate the synthesis and electrochemical performance of polymer-derived silicon oxycarbide–carbon nanotube (SiOC–CNT) composites as a stable lithium intercalation material for secondary battery applications. Composite synthesis was achieved through controlled thermal decomposition of 1,3,5,7-tetramethyl 1,3,5,7-tetravinyl cyclotetrasiloxane (TTCS) precursor on carbon nanotubes surfaces that resulted in formation of shell/core type ceramic SiOC–CNT architecture. Li-ion battery anode (prepared at a loading of $\sim 1.0 \text{ mg cm}^{-2}$) showed stable charge capacity of 686 mA h g^{-1} even after 40 cycles. The average Coulombic efficiency (excluding the first cycle loss) was 99.6%. Further, the post electrochemical imaging of the dissembled cells showed no apparent damage to the anode surface, highlighting improved chemical and mechanical stability of these composites. A similar trend was observed in the rate capability tests, where the SiOC–CNT anode (with 5 wt % loading in TTCS) again showed stable performance, completely recovering the first cycle capacity of $\sim 750 \text{ mA h g}^{-1}$ when the current density was brought back to 50 mA g^{-1} after cycling at higher current densities.



INTRODUCTION

A variety of silicon-based composites are currently being explored as negative electrode materials for lithium ion secondary batteries due to silicon's high lithium alloyability.^{1–4} However, one major issue or limiting factor with silicon-based anodes is the large amount of volume changes associated with insertion and extraction of lithium-ions as the battery is charged/discharged. This results in pulverization (amorphization), cracking (exposing new silicon surface to solvent ions, resulting in formation of an unstable passivating film), and eventual failure of the electrode (due to loss of electrical contact between active material and current collector). To mitigate these effects, several unique hybrid chemistries (that include Si/graphene and Si/carbon nanocomposites) and novel anode architectures (vertically aligned nanowires and core/shell structures) have been proposed that have improved electrochemical cycling in these materials for up to hundreds of cycles.^{5–9} Nonetheless, these nanocomposite anodes (or batteries) usually have low absolute capacities as the amount of active material in the anode has been low (approximately $0.02\text{--}0.1 \text{ mg cm}^{-2}$) and therefore may not be suitable for powering hybrid vehicles or other large devices that require more power and energy (in other words, applications requiring thicker anode).^{10,11}

High temperature glass ceramics prepared from thermal decomposition of certain organosilicon polymers (such as polysiloxanes, polysilazanes, etc.) have been shown to possess many functional properties including their high temperature thermal and chemical stability.^{12–16} A more interesting and recently discovered behavior is their ability to cycle lithium at potentials ranging from 0 to 3 V (versus Li/Li⁺). Recent reports

suggest that this behavior could be due to their “open” amorphous structure, which predominantly consists of $\sim(1\text{--}2)$ nm size domains of silica wrapped by graphitic carbon chains.¹⁶ The presence of nanovoids along with silicon and carbon dangling bonds could also provide ample sites for Li-insertion.^{17,18} Unfortunately, the Si/O/C family of polymer-derived ceramics (PDCs) that shows high Li-intercalation capacity is also the one that is electrically insulating, which ultimately results in poor charge transfer characteristics and voltage hysteresis.^{17–21}

One way to improve the electrochemical performance of Si–O–C-based anodes would be to interface the starting polymeric precursor with conducting fillers such as carbon nanotubes (CNTs), which upon pyrolysis would result in electrical conducting and mechanically robust ceramic-CNT shell/core composite, thereby improving rate capability and resistance to fatigue associated with repeated cycling of Li-ions (particularly for thicker anodes), respectively. Moreover, introduction of CNTs (weight density $\sim 2.3 \text{ g cm}^{-3}$) into SiOC is not likely to affect the overall density of the composite because SiOC weight density also lies in the same range ($\sim 1.8\text{--}2.3 \text{ g cm}^{-3}$), thanks to its “open” amorphous structure.²² Hence, to test this hypothesis, we synthesized core–shell SiOC–CNT composite structure (with varying shell thickness) and studied its electrochemical performance as a working electrode in a Li-ion half-cell. Determination of appropriate amount of CNTs in the composite

Received: October 30, 2012

Revised: May 15, 2013

Published: May 31, 2013

was important as excess amounts of CNTs can result in undesirably high irreversibility, which is typically associated with trapping of Li-ions between the concentric CNT walls.^{23,24}

Material Preparation. The synthesis of SiOC–CNT composite was performed in a manner similar to other PDC–CNT composites described in our recent work.^{25–28} Briefly, the “as-obtained” 1 g of MWCNTs (C150 HP, Bayer AG) was dispersed in 1 g L⁻¹ sodium dodecyl benzene sulfonic acid (NaDDBS) (Sigma Aldrich) aqueous solution, followed by sonication for 1 h to remove any unwanted agglomerations. The dispersed nanotubes were then washed repeatedly with DI water to eliminate any excess NaDDBS or related impurities, followed by slow drying that yielded a dry CNT mass.

These dried nanotubes (approximately 1 g) were then dispersed in toluene (125 mL) for further functionalization with the SiOC polymeric precursor. A mix of commercially sourced 1,3,5,7-tetramethyl 1,3,5,7-tetravinyl cyclotetrasiloxane (TTCS) (Gelest) with 1 wt % dicumyl peroxide (Sigma Aldrich) was then slowly added (predetermined based on MWCNT to TTCS ratio) and stirred in the CNT–toluene dispersion (shown with the help of a schematic in Figure 1). After the mix was stirred

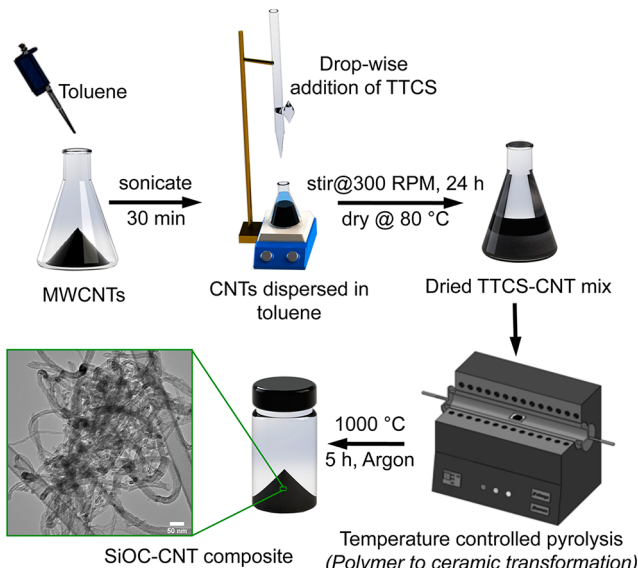


Figure 1. Schematic displaying the stepwise procedure for the synthesis of SiOC (shell)–CNT (core) composite. TTCS is the polymeric precursor for SiOC ceramic.

for approximately 24 h, it was dried in inert atmosphere at 80 °C. The dried mix was then transferred to a tube furnace where it was heated to 400 °C for 4 h for cross-linking of the precursor, followed by a pyrolysis at 1000 °C for 5 h in argon atmosphere at 5 °C min⁻¹ heating and cooling rates to yield SiOC–CNT composite (Figure 1). Three specimens with 5, 8, and 10 wt % of CNTs in TTCS were prepared; these specimens are labeled as SiOC–CNT-5, SiOC–CNT-8, and SiOC–CNT-10, respectively.

The SiOC powder specimen was prepared following standard procedures described in the literature.¹⁶ Briefly, liquid TTCS was cross-linked in a vertical tube furnace at approximately 300 °C in argon for 4 h resulting in an infusible mass, which was ball milled for 2 h and pyrolyzed at 1000 °C for 5 h in Ar resulting in a fine black SiOC powder.

EXPERIMENTAL PROCEDURES

Scanning electron microscopy (SEM) imaging of SiOC–CNT composite bulk and anode specimens was performed by use of a 10 kV Carl Zeiss EVO low-vacuum SEM. Transmission electron microscopy (TEM) was carried out using 100 kV Philips CM 100. Fourier transform infrared (FT-IR) spectra were collected using a liquid nitrogen cooled Thermo-Nicolet Nexus 870 FT-IR spectrometer in the diffuse reflectance mode. The crushed powder specimens were mixed with KBr powder, prior to collecting spectra. X-ray diffraction (XRD) was performed by use of a Bruker D8 Advance powder X-ray diffractometer operating at room temperature, with Cu K α radiation and nickel filter. The pyrolyzed samples were finely crushed with mortar and pestle for analysis. Thermogravimetric analysis (TGA) was performed by use of a Shimadzu 50 TGA (limited to 1000 °C). Sample weighing, approximately 5 mg, was heated in a platinum pan at a rate of 10 °C min⁻¹ in air flowing at 20 mL min⁻¹. Electrochemical characterization of the assembled coin cells was carried out using multichannel Battery Test setup (Arbin-BT2000) at atmospheric conditions.

Half-Cell Assembly and Testing. The synthesized composites were crushed (hand crushed or ball milled) to obtain a fine powder followed by mixing with acetylene black and poly(acrylic acid) as binder in the ratio of 8:1:1 by weight and about the same volume of 1-methyl 2-pyrrolidinone for providing the appropriate viscosity to the slurry. 127 μ m stepped applicator blade was then used to spread the slurry onto a 15 μ m thick copper foil (current collector). The film was then dried at approximately 80 °C overnight in inert conditions. Circles of 9/16" diameter were punched, and the weight of the active material in the film was measured. The 2032 sized coin-cells were then assembled in an argon-filled glovebox. Composite coated on copper foil (punched circle) acted as the working electrode, while pure lithium metal acted as the reference or counter electrode. A monolayer polypropylene membrane (Celgard) soaked in electrolyte acted as the separator between the two electrodes. The electrolyte consisted of 1 M LiPF₆ (Alfa Aesar) lithium salt in (1:1 v/v) dimethyl carbonate (DMC):ethylene carbonate (EC) solvent. The assembled batteries were tested in the voltage range from 10 mV to 2.5 V at constant currents both during discharge (insertion) and charge (extraction) half cycles. The specific capacities mentioned are calculated on the basis of the weight of active material only. Because these ceramics are mostly amorphous and have several energy levels available for Li-insertion/extraction, “C-rate” here is defined (such that it gives time required to insert or extract the charge at a given value of the current) as the ratio of applied current (constant for both charge/discharge) to the observed electrochemical capacity.

RESULTS AND DISCUSSION

The SEM (Figure 2a,d,g) and TEM (Figure 2b,e,h) imaging revealed formation of a shell/core composite nanowire structure with thicker nanowires being formed at lower CNT loading in the polymeric precursor (statistical variation in nanowire diameter is shown in Figure 2c,f,i). For the SiOC–CNT-5 specimen, some aggregated SiOC particles along with SiOC coated CNTs were observed (Figure 2a). The nanotube core was more evident in SiOC–CNT-8 and SiOC–CNT-10 specimens, where the polymeric precursor was perhaps just sufficient to form a monolayer thick SiOC shell on the CNT sidewalls. This increasing amount of nanotubes in the ceramic composite became even more prominent when imaged at higher

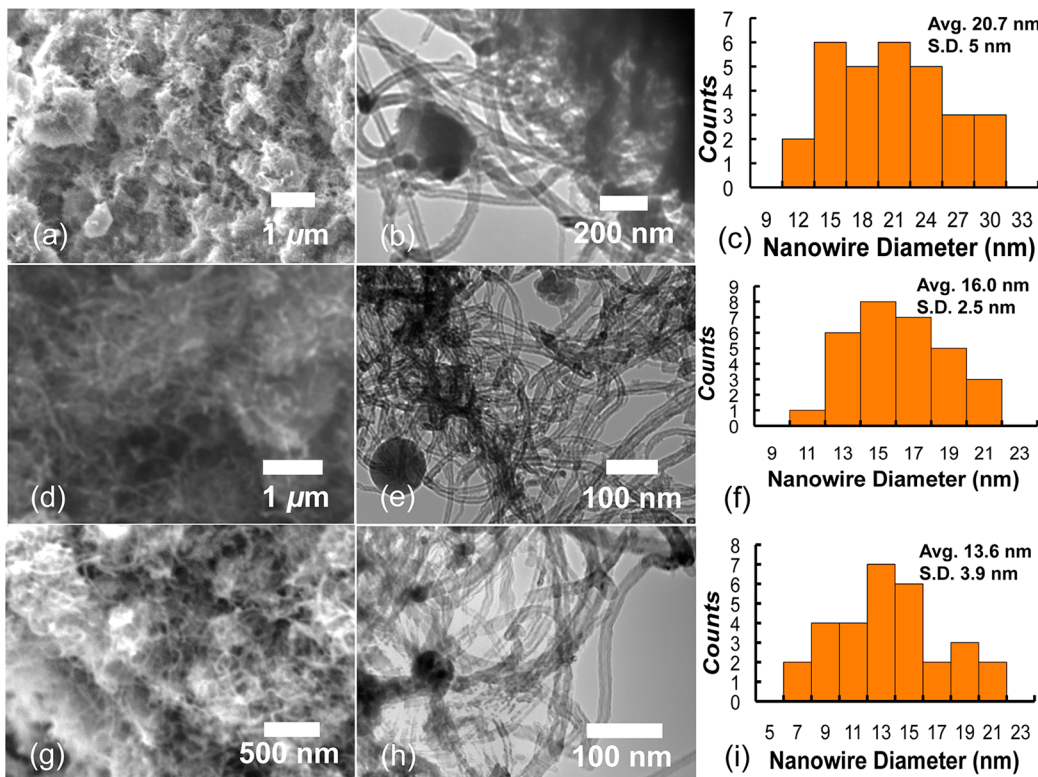


Figure 2. SEM, TEM images and histogram (size distribution) of various SiOC–CNT composites prepared in this study: (a–c) SiOC–CNT-5, (d–f) SiOC–CNT-8, and (g–i) SiOC–CNT-10, respectively. Thicker composite nanowires were observed for composites with lower CNT loading.

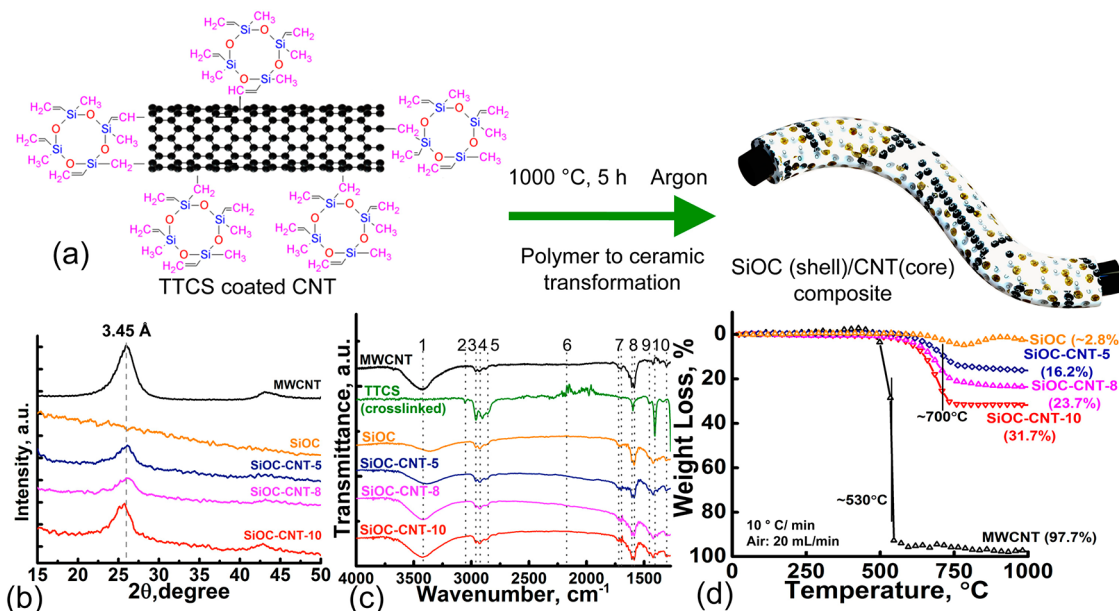


Figure 3. (a) Schematic representation of the molecular level interfacing of TTCS polymeric precursor with CNT sidewalls and resulting transformation to SiOC ceramic shell upon pyrolysis (the schematic is not to scale). (b) XRD data confirming the amorphous nature of polymer-derived SiOC ceramic (hallmark of these materials) and survival of carbon nanotubes in SiOC–CNT composites (peak at ~26°). (c) FTIR spectra showing chemical bond evolution for MWCNTs, cross-linked TTCS polymer, SiOC ceramic, and various SiOC–CNT composite specimens (1, –OH; 2, C–H; 3, C=C; 4, C–H; 5, C–H; 6, Si–H; 7, C=C; 8, Si–CH₃; 9, Si–CH₃; 10, Si–O). Polymer to ceramic conversion generally involves breaking of Si–H and Si–CH₃ bonds with release of hydrogen and other volatile species such as CO₂, CH₄, H₂O, etc., and (d) TGA data for determination of weight percent of CNTs in final composite.

magnifications in a TEM (Figure 2b,e,h). The polymer to ceramic transformation on the surface of a carbon nanotube is shown with the help of a schematic in Figure 3a. Further, XRD results confirmed that the ceramic was indeed amorphous when

processed at 1000 °C, which is one of the hallmarks of PDCs (Figure 3b).

The FT-IR spectroscopy of SiOC and SiOC–CNT specimens (Figure 3c) showed stretching of –OH (3423 cm⁻¹), Si–H

(2314 cm^{-1}), Si—O—C (1384 cm^{-1}), and C—H ($2917\text{--}2877\text{ cm}^{-1}$) and bending of Si—CH₃ (1607, 1585, and 1420 cm^{-1}) bonds. The polymer to ceramic transformation involves breaking of Si—CH₃ and C—H bonds, and this effect is clearly captured in the FTIR spectrum with the decrease in the intensity of corresponding peaks. These results are also in agreement with other studies on bulk polymer-derived SiOC ceramics. Moreover, the presence of CNTs in the composite could be observed as C=C stretching at 1722 cm^{-1} (due to its pristine nature) and C—H stretching at 2864 cm^{-1} (possibly due to defect sites). The chemical interaction of SiOC with CNT sidewall could not be confirmed with these techniques. However, on the basis of the present analysis, physical adhesion of SiOC ceramic on CNT surface can be safely predicted.

Further, TGA measurements were performed (in flowing air) to ascertain the amount of ceramic present in the composite. As expected, more ceramic was observed in SiOC—CNT-5 specimen than SiOC—CNT-10 (Figure 3d). Moreover, all SiOC—CNT composite specimens showed higher oxidation resistance ($\sim 700\text{ }^{\circ}\text{C}$) than pure MWCNTs ($\sim 530\text{ }^{\circ}\text{C}$), which suggests protection of nanotube core by the ceramic shell. TGA data for pure SiOC have also been included for comparison.

Now, assuming that the SiOC polymeric precursor uniformly covers the entire CNT surface, ceramic shell thickness can be approximated using the following relationship:²⁹

$$\text{ML}_{\text{SiOC}} = \frac{w_{\text{SiOC}}}{1 - w_{\text{SiOC}}} \times \frac{\text{MW}_{\text{CNT}}}{\text{MW}_{\text{SiOC}}} \times \left(\frac{\Omega_{\text{SiOC}}}{\Omega_{\text{CNT}}} \right)^{2/3} \quad (1)$$

where ML_{SiOC} are the number of SiOC monolayers on CNT, and w_{SiOC} is the weight fraction of SiOC in the composite determined experimentally by TGA to be 84, 76, and 68 (for SiOC—CNT-5, SiOC—CNT-8, and SiOC—CNT-10, respectively, Table 1).

Table 1. Summary of the TGA Data^a

specimen	wt % of CNTs in TTCS	oxidation temp	residual weight (%)	calculated wt % of CNTs in SiOC	calculated monolayers of SiOC
MWCNTs		536.2	2.3		
SiOC		746.8	97.2		
SiOC—CNT-5	5	714.8	83.8	16.2	3.04
SiOC—CNT-8	8	704.1	76.3	23.7	1.89
SiOC—CNT-10	10	693.7	68.3	31.7	1.23

^aWeight percent of CNTs in SiOC is calculated on the basis of the residual weight. All weight values in the table are accurate up to 0.1%.

Molecular weights MW_{CNT} and MW_{SiOC} are 12 and 56 g mol^{-1} , and Ω is the ratio of molar volume/Avogadro's number for CNT and SiOC. TEM images seem to corroborate these results as the SiOC—CNT-5 specimen was observed to be considerably thicker than SiOC—CNT-8 and SiOC—CNT-10 specimens.

We then studied the long-term electrochemical cycling of five specimen types including SiOC, MWCNTs, and three SiOC—CNT composite specimens. The first and second cycle discharge and charge plots are shown in Figure 4. Figure 4a and c represents SiOC and MWCNT anode, while Figure 4e–i shows SiOC—CNT composite anodes, respectively. The best performance was observed for SiOC—CNT-5 specimen, which showed a first cycle reversible capacity of 841.8 mA h g^{-1} with a first cycle efficiency of 67.1%.

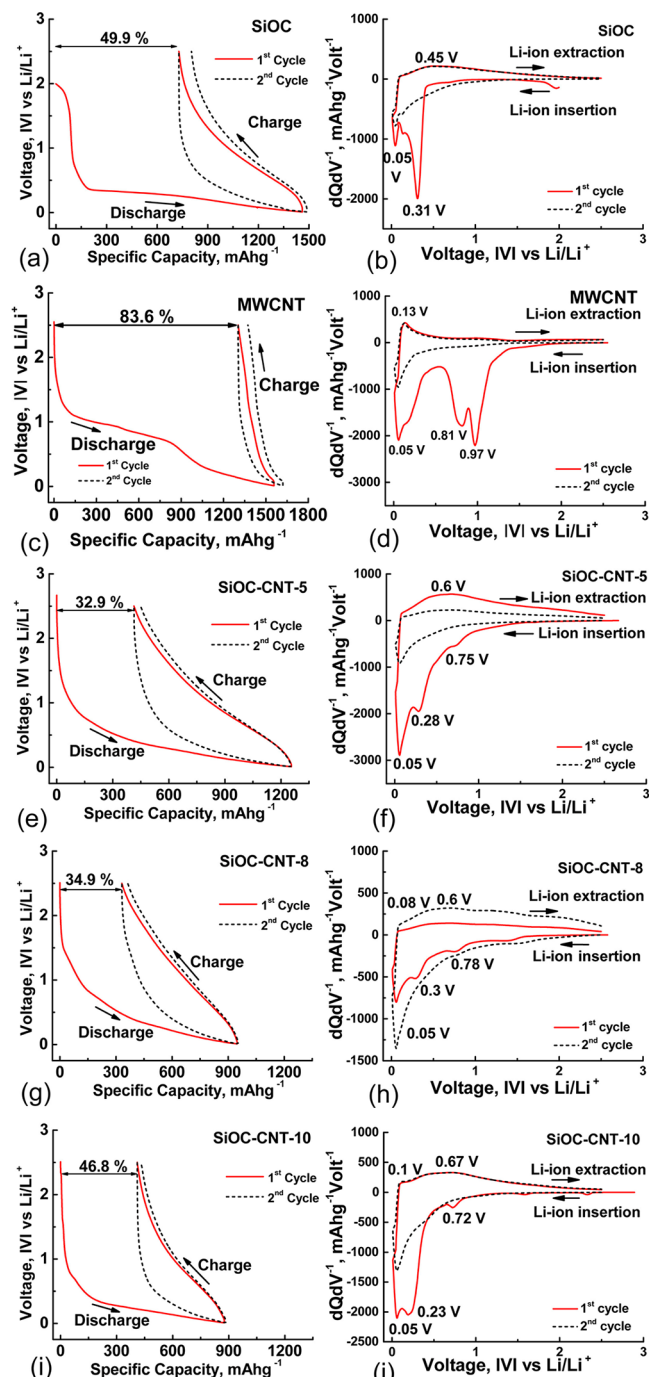


Figure 4. Electrochemical data for various SiOC anodes used in this study: (a,c,e,g) First and second charge/discharge profiles for SiOC, MWCNT, SiOC—CNT-5, SiOC—CNT-8, and SiOC—CNT-10, respectively. (b,d,f,h,j) Differentiated capacity versus voltage plot for SiOC, MWCNT, SiOC—CNT-5, SiOC—CNT-8, and SiOC—CNT-10, respectively.

The differentiated capacity curves (i.e., dQ/dV versus voltage) for the first two cycles for SiOC (Figure 4b), MWCNTs (Figure 4d), and various SiOC—CNT (Figure 4f,h,j) anodes are plotted next to their cycling plots. The reduction peaks are categorized as (I) at $\sim 0.05\text{ V}$, (II) between (0.25 and 0.33) V, and (III) at $\sim 0.7\text{ V}$, while oxidation peaks are categorized as (IV) $\sim 0.1\text{ V}$ and (V) $\sim 0.6\text{ V}$. The reduction at $\sim 0.05\text{ V}$ seems to originate from Li-intercalation in "graphitic carbon", which is present in both pristine SiOC ceramic and MWCNTs.^{18,30} The

Table 2. Summary of the Electrochemical Data and Comparison with Results from Literature

specimen	first cycle charge capacity (mA h g ⁻¹)	first cycle loss (%)	first cycle Coulombic efficiency (%)	charge capacity after "n" cycles (mA h g ⁻¹)	% capacity retention after "n" cycles	average Coulombic efficiency (%) after "n" cycles ^a
C-rich-SiOC ²⁰	241	60.5	39.5	150 (30)	55.9 (30)	N/A
MWCNTs ²³	210	56.2	43.8	220 (20)	104.7 (20)	N/A
MWCNTs	255	83.6	16.3	250.6 (40)	101.7 (40)	99.2 (40)
SiOC	731.5	49.9	50.1	456.2 (40)	62.4 (40)	99.2 (40)
SiOC-CNT-5	841.8	32.9	67.1	686.3 (40)	81.5 (40)	99.6 (40)
SiOC-CNT-8	620.1	34.9	65.1	525.8 (40)	84.8 (40)	99.4 (40)
SiOC-CNT-10	465.9	46.8	53.2	459.6 (40)	98.6 (40)	99.6 (40)

^aSecond cycle onward.

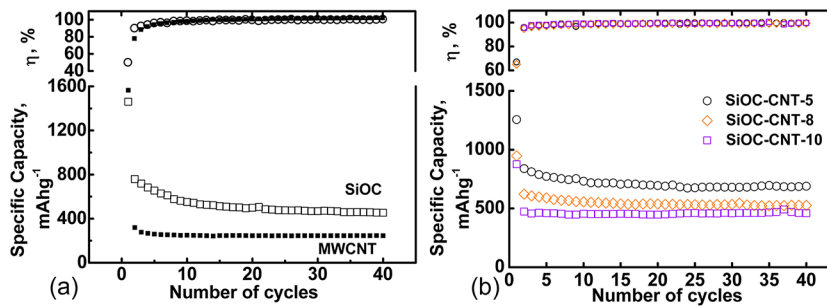


Figure 5. (a) Specific discharge capacity and efficiency of the SiOC and MWCNTs anodes tested for 40 cycles. (b) Specific discharge capacity and efficiency of SiOC-CNT composite anode specimens cycled for 40 cycles at ~C/10.

reduction peak at ~ 0.3 V is most likely due to Li-intercalation in nanovoids or chemical bonding with dangling bonds present at Si and C sites in the ceramic.³¹ One other reduction peak at ~ 0.7 – 0.8 V was seen only in the first cycle for SiOC-CNT anodes (absent in SiOC) and is characteristic of electrolyte decomposition (formation of passivating solid electrolyte interphase layer) for MWCNTs-based anodes with LiPF₆-based electrolytes.^{23,24} The Li-ion oxidation peaks at ~ 0.1 V correspond to graphitic carbon present in SiOC and MWCNT.^{23,32} For these specimens, the dQ/dV^{-1} plot in the second cycle showed an intense reduction peak-I (at 0.05 V), while a weaker oxidation peak-V (0.5 V) was observed for all of the specimens. This implies that (a) multiple phases (energy levels) in SiOC-CNT seem to contribute toward lithium intercalation, and (b) Li-ion intercalation in SiOC ceramic phases start to dominate over the MWCNT after the first electrochemical cycle is over.

High first cycle irreversibility in MWCNTs is typical and is attributed to Li-trapping between their intertubular spacing ($>56\%$).^{23,24} Thus, increasing amounts of CNTs (5, 8, and 10 wt %) in SiOC composites could be directly correlated to the increasing first cycle loss (ICL) of 32.9%, 34.9%, and 46.8% in the specimen performance. Additionally, as shown in Table 1, in SiOC-CNT-5 specimen the SiOC coating thickness on MWCNTs (~ 3 layers) can reduce the Li-ion diffusion into the CNT core and thereby limit the entrapment of Li-ions inside nanotubes as compared to the SiOC-CNT-10 specimen (~ 1 layer of SiOC on CNT). Remarkably, the cycling efficiency in the SiOC-CNT specimens was observed to be consistently at 99% or above, which can be collectively attributed to the stable SiOC ceramic shell that surrounds the conducting nanotube core resulting in efficient uptake and desorption of Li-ions. The reversible capacity and the first cycle efficiency of SiOC-CNT composites reported here (Table 2) are higher than those of some other PDC-based anodes.^{30,33–35} For example, porous SiOC has been reported to have first cycle reversible (charge) capacity of ~ 272 mA h g⁻¹ (59% efficiency),²⁰ SiCN at ~ 374 mA

h g⁻¹ (74% efficiency),³⁰ SiCN-graphite composite at ~ 474 mA h g⁻¹ (64.8% efficiency),³⁴ and Si(B)CN-CNT at 241.9 mA h g⁻¹ (41% efficiency).³⁵

Long-term cycling performance of SiOC and all SiOC-CNT specimens is plotted in Figure 5a and b, respectively. High capacity retention in these anodes is good evidence of their chemical and structural stability induced by ceramic shell and nanotube core, respectively. For the SiOC anode, the capacity dropped by approximately 44% after 40 cycles. SiOC-CNT specimens showed exceptional specific capacity retention with SiOC-CNT-10 leading with 98.6% (at 459.6 mA h g⁻¹) followed by SiOC-CNT-8 with 84.8% (at 525.8 mA h g⁻¹) and SiOC-CNT-5 with 81.5% (at 686.3 mA h g⁻¹) after 40 cycles. These results suggest improved mechanical toughness of the anode due to inclusion of CNTs.

In addition, we also note that the polysiloxane derived SiOC ceramics processed at 1000 °C are electrically insulating ($<10^{-12}$ S cm⁻¹).¹⁹ Pellets of SiOC-CNT composite powder prepared by cold pressing (approximately 4 kpsi) showed electrical conductivities in the range of 1.2×10^{-5} S cm⁻¹ (SiOC-CNT-5) to 6.05×10^{-5} S cm⁻¹ (SiOC-CNT-10). Thus, CNTs play an important role both in providing an electrical connection within the anode and in binding the active SiOC particles as one unit.

Furthermore, a recent study on Si-O-C ceramic anodes suggests formation of oxygen as well as carbon-rich Si_xO_yC_z phases during Li-ion intercalation.³⁶ The dominant oxygen-rich phases like SiO₂C₂, SiO₃C, and SiO₄ were observed to facilitate a reversible reaction with Li-ions, while carbon-rich phases of SiOC₃ and SiC₄ were suggested to result in nonreversible reactions with lithium. It is likely that oxygen-rich phases could be more dominant in SiOC-CNT-5 specimen than others, resulting in lower first cycle loss. Nonetheless, further studies involving in situ NMR could provide more insights into these composite materials and are currently beyond the scope of the present work.

Later, post electrochemical imaging was carried out on disassembled anodes to observe any signs of fatigue, crack formation, film delamination, or pulverization that is typical in case of silicon-based anode when subjected to long-term electrochemical cycling. The process involved disassembling the batteries and recovering the anode by repeated rinsing in DMC to clean the surface contaminants. The whole process was carried out in an argon-filled glovebox, and the recovered anodes were then instantly transferred to SEM for imaging. As seen in Figure 6, all cycled anodes except SiOC (Figure 6a,b) displayed uniform

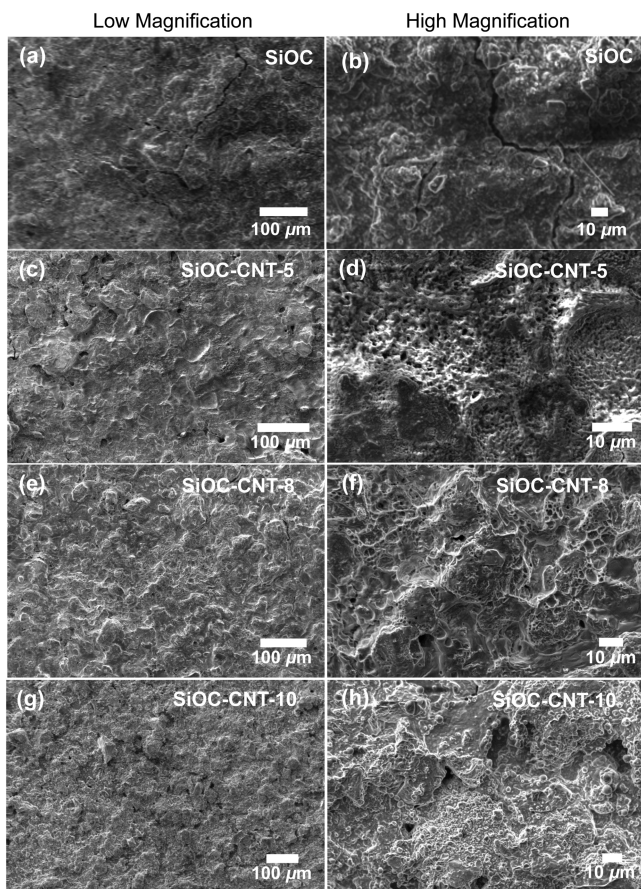


Figure 6. SEM micrographs (left, low magnification; right, high magnification) of various disassembled anode specimen after testing for 40 cycles, (a,b) SiOC (active anode weight: 1.4 mg), (c,d) SiOC–CNT-5 (active anode weight: 1.4 mg), (e,f) SiOC–CNT-8 (active anode weight: 1.5 mg), and (g,h) SiOC–CNT-10 (active anode weight: 1.6 mg). All anodes were approximately 127 μm thick.

interconnected particle like appearance with uniform surface morphology and a stable coating. Crack-free SEI was observed on all SiOC–CNT anode surfaces (Figure 6c–h). Degradation like delamination of active material and stress cracks due to volume expansion/contraction were also not seen. High magnification images of SiOC anode showed that the particles were loosely held with a few micrometer size cracks being formed, which may be the reason for its reduced electrochemical capacity with increasing cycle number.

Last, the rate capability tests were performed (Figure 7), where the anodes were cycled for five cycles each at increasing current densities of 50, 100, 200, 400, 800, and 1600 mA g^{-1} and then back at 50 mA g^{-1} . Similar to previous observations, here also the SiOC–CNT anodes showed better stability than bulk SiOC

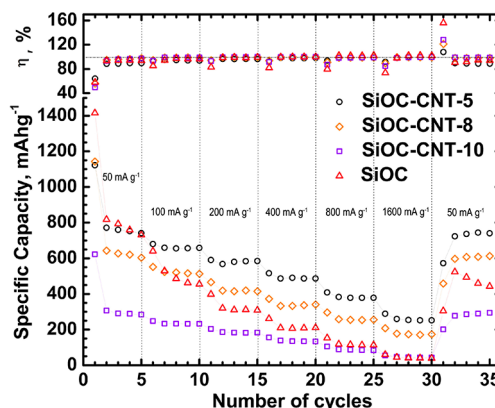


Figure 7. Rate capability test data for SiOC, SiOC–CNT-5, SiOC–CNT-8, and SiOC–CNT-10 anode specimens showing specific discharge capacity and columbic efficiency. All SiOC–CNT anodes showed stable performance with SiOC–CNT-5 showing best overall cyclability.

anode. Among these, the SiOC–CNT-5 specimen showed highest specific capacity of $\sim 750 \text{ mA h g}^{-1}$, which was fully recovered when the current density was brought back to 50 mA g^{-1} . In addition, we also cycled and compared the performance of SiOC–CNT-2.5 anode specimen with SiOC and SiOC–CNT-5 specimen (see Supporting Information, Figure S1). Here, also the SiOC–CNT-5 specimen (with specific capacity of $\sim 260 \text{ mA h g}^{-1}$ at 1600 mA g^{-1}) consistently outperformed SiOC–CNT-2.5 (specific capacity of $\sim 46 \text{ mA h g}^{-1}$ at 1600 mA g^{-1}), suggesting that 5 wt % loading of MWCNT in TTCS is necessary for achieving optimum performance in these composite nanowires.

In conclusion, we have demonstrated the synthesis of polymer-derived SiOC–CNT composites with varying nanotube contents. Infrared spectroscopy revealed the presence of Si–O, Si–O–Si, Si–H, and C=C bonds from SiOC and C=C and C–H from CNTs, suggesting conversion of TTCS polymer to ceramic on nanotube surfaces. These composites demonstrated stable performance and good rate capability with Li-ions when used as battery anode. SiOC–CNT specimen prepared from pyrolysis of 5 wt % CNTs in TTCS exhibited the best performance in terms of specific capacity ($686.3 \text{ mA h g}^{-1}$), while capacity retention was 81.5% after 40 cycles. More importantly, these anodes reached Coulombic efficiencies close to 99% within the first few cycles. Further, the differentiated capacity curves (dQ/dV^{-1}) revealed capacity contribution from $-sp^2$ carbon in CNTs as well as SiOC ceramic (low voltage peak at $\sim 0.05 \text{ V}$), while a separate peak between 0.2 and 0.3 V seems to emerge from lithiation at nanovoids or chemical bonding with silicon/carbon dangling bonds in SiOC ceramic. The post cycling imaging of the composite anode surface revealed the formation of a stable passivating film (improved chemical stability) with no signs of mechanical cracking or delamination (improved mechanical toughness).

ASSOCIATED CONTENT

Supporting Information

Electrochemical cyclability test data comparing SiOC, SiOC–CNT-2.5, and SiOC–CNT-5 anode specimens showing specific discharge capacity and columbic efficiency. This material is available free of charge via the Internet at <http://pubs.acs.org>.

AUTHOR INFORMATION

Corresponding Author

*Tel.: 785-532-7085. Fax: 785-532-7057. E-mail: gurpreet@ksu.edu.

Notes

The authors declare no competing financial interest.

ACKNOWLEDGMENTS

G.S. would like to thank Kansas State University for start-up funds. We would like to thank Mr. Lamuel David for help with specimen preparation. Thanks are also due to Professor Rishi Raj (University of Colorado at Boulder) and Dr. Dongjoon Ahn (GM Research, Warren, MI) for introducing us to lithium-ion battery research.

REFERENCES

- (1) Liu, X. H.; Zhong, L.; Huang, S.; Mao, S. X.; Zhu, T.; Huang, J. Y. Size-Dependent Fracture of Silicon Nanoparticles During Lithiation. *ACS Nano* **2012**, *6*, 1522–1531.
- (2) Krishnan, R.; Lu, T.; Koratkar, N. Functionally Strain-Graded Nanoscoops for High Power Li-Ion Battery Anodes. *Nano Lett.* **2011**, *11*, 377–384.
- (3) Kim, H.; Cho, J. Superior Lithium Electroactive Mesoporous Si@Carbon Core–Shell Nanowires for Lithium Battery Anode Material. *Nano Lett.* **2008**, *8*, 3688–3691.
- (4) Yao, Y.; McDowell, M. T.; Ryu, I.; Wu, H.; Liu, N.; Hu, L.; Nix, W. D.; Cui, Y. Interconnected Silicon Hollow Nanospheres for Lithium-Ion Battery Anodes with Long Cycle Life. *Nano Lett.* **2011**, *11*, 2949–2954.
- (5) Luo, J.; Zhao, X.; Wu, J.; Jang, H. D.; Kung, H. H.; Huang, J. Crumpled Graphene-Encapsulated Si Nanoparticles for Lithium Ion Battery Anodes. *J. Phys. Chem. Lett.* **2012**, *3*, 1824–1829.
- (6) Cui, L.; Ruffo, R.; Chan, C. K.; Peng, H.; Cui, Y. Crystalline-Amorphous Core–Shell Silicon Nanowires for High Capacity and High Current Battery Electrodes. *Nano Lett.* **2009**, *9*, 491–495.
- (7) Hwang, T. H.; Lee, Y. M.; Kong, B.; Seo, J.; Choi, J. W. Electrospun Core–Shell Fibers for Robust Silicon Nanoparticle-Based Lithium Ion Battery Anodes. *Nano Lett.* **2012**, *12*, 802–807.
- (8) Magasinski, A.; Dixon, P.; Hertzberg, B.; Kvitt, A.; Ayala, J.; Yushin, G. High-Performance Lithium-Ion Anodes Using a Hierarchical Bottom-Up Approach. *Nat. Mater.* **2010**, *9*, 353–358.
- (9) Hertzberg, B.; Alexeev, A.; Yushin, G. Deformations in Si–Li Anodes Upon Electrochemical Alloying in Nano-Confining Space. *J. Am. Chem. Soc.* **2010**, *132*, 8548–8549.
- (10) Chan, C. K.; Peng, H.; Liu, G.; McIlwrath, K.; Zhang, X. F.; Huggins, R. A.; Cui, Y. High-Performance Lithium Battery Anodes Using Silicon Nanowires. *Nat. Nanotechnol.* **2008**, *3*, 31–35.
- (11) Xilin, C. X.; Li, X.; Ding, F.; Xu, W.; Xiao, J.; Cao, Y.; Meduri, P.; Liu, J.; Graff, G.; Zhang, J. Conductive Rigid Skeleton Supported Silicon as High-Performance Li-Ion Battery Anodes. *Nano Lett.* **2012**, *12*, 4124–30.
- (12) Sarkar, S.; Gan, Z.; An, L.; Zhai, L. Structural Evolution of Polymer-derived Amorphous SiBCN Ceramics at High Temperature. *J. Phys. Chem. C* **2011**, *115*, 24993–25000.
- (13) Pena-Alonso, R.; Mariotto, G.; Gervais, C.; Babonneau, F.; Soraru, G. D. New Insights on the High-Temperature Nanostructure Evolution of SiOC and B-Doped SiBOC Polymer-Derived Glasses. *Chem. Mater.* **2007**, *19*, 5694–5702.
- (14) Soraru, G. D.; Suttor, D. High Temperature Stability of Sol-Gel-Derived SiOC Glasses. *J. Sol.-Gel Sci. Technol.* **1999**, *14*, 69–74.
- (15) Sarkar, S.; Zou, J. H.; Liu, J. H.; Xu, C. Y.; An, L. A.; Zhai, L. Polymer-Derived Ceramic Composite Fibers with Aligned Pristine Multiwalled Carbon Nanotubes. *ACS Appl. Mater. Interfaces* **2010**, *2*, 1150–1156.
- (16) Saha, A.; Raj, R.; Williamson, D. L. A Model for the Nanodomains in Polymer-Derived SiCO. *J. Am. Ceram. Soc.* **2006**, *89*, 2188–2195.
- (17) Fukui, H.; Nakata, N.; Dokko, K.; Takemura, B.; Ohsuka, H.; Hino, T.; Kanamura, K. Lithiation and Delithiation of Silicon Oxycarbide Single Particles With a Unique Microstructure. *ACS Appl. Mater. Interfaces* **2011**, *3*, 2318–2322.
- (18) Shen, J.; Raj, R. Silicon-Oxycarbide Based Thin Film Anodes For Lithium Ion Batteries. *J. Power Sources* **2011**, *196*, 5945–5950.
- (19) Cordelair, J.; Greil, P. Electrical Conductivity Measurements as a Microprobe For Structure Transitions in Polysiloxane Derived Si–O–C Ceramics. *J. Eur. Ceram. Soc.* **2000**, *20*, 1947–1957.
- (20) Dibandjo, P.; Graczyk-Zajac, M.; Riedel, R.; Pradeep, V. S.; Soraru, G. D. Lithium Insertion into Dense and Porous Carbon-Rich Polymer-Derived SiOC Ceramics. *J. Eur. Ceram. Soc.* **2012**, *32*, 2495–2503.
- (21) Xing, W.; Wilson, A. M.; Eguchi, K.; Zank, G.; Dahn, J. R. Pyrolyzed Polysiloxanes for Use as Anode Materials in Lithium-Ion Batteries. *J. Electrochem. Soc.* **1997**, *144*, 2410–2416.
- (22) Colombo, P.; Mera, G.; Riedel, R.; Soraru, G. D. Polymer-Derived Ceramics: 40 Years of Research and Innovation in Advanced Ceramics. *J. Am. Ceram. Soc.* **2010**, *93* (7), 1805–1837.
- (23) Landi, B. J.; DiLeo, R. A.; Schauerman, C. M.; Cress, C. D.; Ganter, M. J.; Raffaele, R. P. Multi-walled Carbon Nanotube Paper Anodes for Lithium Ion Batteries. *J. Nanosci. Nanotechnol.* **2009**, *2*, 3406–3410.
- (24) Frackowiak, E.; Gautier, S.; Gaucher, H.; Bonnamy, S.; Beguin, F. Electrochemical Storage of Lithium in Multiwalled Carbon Nanotubes. *Carbon* **1999**, *37*, 61–69.
- (25) Bhandavat, R.; Kuhn, W.; Mansfield, E.; Lehman, J.; Singh, G. Synthesis of Polymer-Derived Ceramic Si(B)CN-Carbon Nanotube Composite by Microwave-Induced Interfacial Polarization. *ACS Appl. Mater. Interfaces* **2012**, *4*, 11–16.
- (26) Bhandavat, R.; Singh, G. Synthesis, Characterization, and High Temperature Stability of Si(B)CN-Coated Carbon Nanotubes Using a Boron-Modified Poly(ureamethylvinyl)Silazane Chemistry. *J. Am. Ceram. Soc.* **2012**, *95*, 1536–1543.
- (27) Lehman, J. H.; Hurst, K. E.; Singh, G.; Mansfield, E.; Perkins, J. D.; Cromer, C. L. Core–Shell Composite of SiCN and Multiwalled Carbon Nanotubes From Toluene Dispersion. *J. Mater. Sci.* **2010**, *45*, 4251–4254.
- (28) Bhandavat, R.; Feldman, A.; Cromer, C.; Lehman, J.; Singh, G. Very High Laser-Damage Threshold of Polymer-derived Si(B)CN-Carbon Nanotube Composite Coatings. *ACS Appl. Mater. Interfaces* **2013**, *5*, 2354–2359.
- (29) Shah, S. R.; Raj, R. Nanodevices That Explore The Synergies Between PDCs and Carbon Nanotubes. *J. Eur. Ceram. Soc.* **2005**, *25*, 243–249.
- (30) Graczyk-Zajac, M.; Fasel, C.; Riedel, R. Polymer-derived-SiCN Ceramic/Graphite Composite as Anode Material With Enhanced Rate Capability For Lithium Ion Batteries. *J. Power Sources* **2011**, *196*, 6412–6418.
- (31) Chan, C. K.; Ruffo, R.; Hong, S. S.; Huggins, R. A.; Cui, Y. Structural and Electrochemical Study of the Reaction of Lithium with Silicon Nanowires. *J. Power Sources* **2009**, *189*, 34–39.
- (32) Graczyk-Zajac, M.; Toma, L.; Fasel, C.; Riedel, R. Carbon-rich SiOC Anodes for Lithium-Ion Batteries: Part I. Influence of Material UV-Pre-treatment on High Power Properties. *Solid State Ionics* **2012**, *225*, 522–526.
- (33) Feng, Y.; Du, G.; Zhao, X.; Yang, E. Preparation and Electrochemical Performance of SiCN–CNTs Composite Anode Material for Lithium Ion Batteries. *J. Appl. Electrochem.* **2011**, *41*, 999–1002.
- (34) Kolb, R.; Fasel, C.; Liebau-Kunzmann, V.; Riedel, R. SiCN/C-Ceramic Composite as Anode Material for Lithium Ion Batteries. *J. Eur. Ceram. Soc.* **2006**, *26*, 3903–3908.
- (35) Bhandavat, R.; Singh, G. Improved Electrochemical Capacity of Precursor-Derived Si(B)CN-Carbon Nanotube Composite as Li-Ion Battery Anode. *ACS Appl. Mater. Interfaces* **2012**, *4*, 5092–5097.
- (36) Liu, X.; Zheng, M.; Xie, K. Mechanism of Lithium Storage in Si–O–C Composite Anodes. *J. Power Sources* **2011**, *196*, 10667–10672.